ATLAS NOTE

ATLAS-CONF-2015-001

February 10, 2015

Search for exotic Higgs-boson decays in events with at least one photon, missing transverse momentum, and two forward jets produced in $\sqrt{s} = 8$ TeV pp collisions with the ATLAS detector

The ATLAS Collaboration

ATLAS-CONF-2015-001
12 February 2015

Abstract

A search is performed for Higgs-boson decays to neutralinos and/or gravitinos in events with at least one photon, missing transverse momentum and two forward jets, a topology where vector boson fusion production is enhanced. The analysis is based on a dataset of proton-proton collision data taken at $\sqrt{s} = 8$ TeV delivered by the Large Hadron Collider and recorded with the ATLAS detector, corresponding to an integrated luminosity of 20.3 fb^{-1}. The observation is consistent with Standard Model expectation and upper limits are set on the production cross section times branching fraction of the Higgs-boson to decay to neutralinos and/or gravitinos.

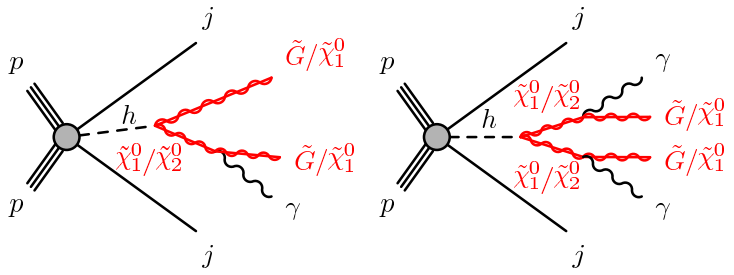

Figure 1: Diagrams for the production and decay of the Higgs-boson leading to (a) the $\gamma + E_{\mathrm{T}}^{\mathrm{miss}} + jj$ final state and (b) the $\gamma\gamma + E_{\mathrm{T}}^{\mathrm{miss}} + jj$ final state. Such signals are predicted by GMSB ($h \to \tilde{G}\,\tilde{\chi}^0 \to \tilde{G}\,\tilde{G}\,\gamma$ or $h \to \tilde{\chi}^0\,\tilde{\chi}^0 \to \tilde{G}\,\gamma\,\tilde{G}\,\gamma$) and NMSSM ($h \to \tilde{\chi}_2^0\,\tilde{\chi}_1^0 \to \tilde{\chi}_1^0\,\tilde{\chi}_1^0\,\gamma$ or $h \to \tilde{\chi}_2^0\,\tilde{\chi}_2^0 \to \tilde{\chi}_1^0\,\gamma\,\tilde{\chi}_1^0\,\gamma$) models.

1 Introduction

A particle consistent with the Standard Model (SM) Higgs-boson (h) was observed by the ATLAS [1] and CMS [2] collaborations in 2012. The Higgs-boson was observed in various SM channels, and the observed data was fit to obtain the coupling constants to SM fermions and gauge bosons. These fits help constrain the branching fraction (BF) of the Higgs-boson to beyond-the Standard Model (BSM) particles [3]. Depending on the Higgs-boson production cross section, BF(h →BSM) could be O(50%) [4]. Supersymmetric (SUSY) [5–13] extensions to the SM can explain the mass of the Higgs-boson and address the hierarchy problem [14–19]. In certain extensions the Higgs-boson is predicted to decay into SUSY particles. Specifically, a class of gauge mediated supersymmetry breaking (GMSB) models [20–25] predict a Higgs-boson decay to a nearly massless gravitino $\tilde{G}$ (the lightest supersymmetric particle, LSP) and a neutralino $\tilde{\chi}^0$ (the next-to-lightest supersymmetric particle, NLSP), where the mass of the neutralino is between half the Higgs-boson mass and the Higgs-boson mass ($m_h/2 < m_{\tilde{\chi}^0} < m_h$) [26]. The neutralino decays to a photon (γ) and a gravitino, which escapes detection and leads to a signature of γ + missing transverse momentum (whose magnitude is denoted E_T^{miss}). In GMSB models, many mechanisms exist [27–31] to generate a Higgs-boson mass compatible with that observed, without changing the phenomenology of the models considered in this search. Next-to-Minimal Supersymmetric Standard Models (NMSSM) [32] also predict a $\gamma + E_T^{\mathrm{miss}}$ signature where the Higgs-boson decays to the next-to-lightest neutralino $\tilde{\chi}_2^0$ (NLSP) and the lightest neutralino $\tilde{\chi}_1^0$ (LSP), and the $\tilde{\chi}_2^0$ decays to a photon and a $\tilde{\chi}_1^0$. This decay chain also occurs when $m_h/2 < m_{\tilde{\chi}_2^0} < m_h$. In the NMSSM, the mass difference between the dominantly bino-like NLSP and singlino-like LSP is more free, when compared to the MSSM [4]. The GMSB and NMSSM decays leading to this signature are shown in Fig. 1 (a). The case where $m_{\tilde{\chi}^0} < m_h/2$ (or $m_{\tilde{\chi}_2^0} < m_h/2$) is also considered, which leads to a diphoton + E_T^{miss} signature, as shown in Fig. 1 (b). The analysis is optimized for the $\gamma + E_T^{\mathrm{miss}}$ signature.

For Higgs-boson production via vector-boson-fusion (VBF), the Higgs-boson is produced along with two jets. These "VBF jets" are widely separated in pseudorapidity η[1] and have a high di-jet invariant mass, m_{jj}. In the VBF topology, the Higgs-boson is often boosted in the transverse plane, forcing the decay products to be closer to each other, so the photon and $E_{\mathrm{T}}^{\mathrm{miss}}$ are not necessarily back-to-back. Additional variables, such as the angles between the VBF jets, the photon, and the $E_{\mathrm{T}}^{\mathrm{miss}}$, can be used

[1]The ATLAS reference system is a Cartesian right-handed coordinate system, with nominal collision point at the origin. The anti-clockwise beam direction defines the positive z-axis, with the x-axis pointing to the center of the LHC ring. The pseudorapidity is defined as η = -ln(tan(θ/2), where the polar angle θ is taken with respect to the positive z direction.

to reduce backgrounds and define control regions to measure backgrounds using the data. In gluon-gluon fusion (ggF) Higgs-boson production, the Higgs-boson is typically produced at lower transverse momentum (p_T), so the photon and the $E_{\mathrm{T}}^{\mathrm{miss}}$are more back-to-back in the transverse plane. This final state is dominated by γ+jet and multijet backgrounds, and electroweak backgrounds (mainly W boson decays to $e\nu$, where the electron is misidentified as a photon). Furthermore, in the ggF topology, it is more difficult to define control regions to accurately measure the γ+jets and multijet backgrounds. Therefore this analysis searches for Higgs-boson decays to neutralinos and/or gravitinos using the VBF topology. A cut-and-count experiment is performed and the total number of expected background and signal events in the control and signal regions are used to set limits on $(\sigma/\sigma_{SM}) \times$ BF($h \rightarrow$ NLSP + LSP).

2 The ATLAS detector

ATLAS is a multipurpose particle physics experiment [33]. It consists of a detector with forward-backward symmetric cylindrical geometry. The Inner Detector (ID) covers $|\eta|$ <2.5 and consists of a silicon pixel detector, a semiconductor microstrip detector, and a transition radiation tracker. The ID is surrounded by a thin superconducting solenoid providing a 2 T axial magnetic field. A high-granularity lead/liquid-argon (LAr) sampling calorimeter measures the energy and the position of electromagnetic showers within $|\eta| < 3.2$. Sampling calorimeters with LAr are also used to measure hadronic showers in the end-cap ($1.5 < |\eta| < 3.2$) and forward ($3.1 < |\eta| < 4.9$) regions, while a steel/scintillator tile calorimeter measures hadronic showers in the central region ($|\eta| < 1.7$). The muon spectrometer (MS) surrounds the calorimeters and consists of three large superconducting air-core toroid magnets, each with eight coils, a system of precision tracking chambers ($|\eta| < 2.7$), and fast trigger chambers ($|\eta| < 2.4$). A three-level trigger system consisting of Level 1, Level 2 and Event Filter (EF) levels, selects events to be recorded for permanent storage.

3 Monte Carlo simulation

The Higgs-boson signal Monte Carlo (MC) samples are generated using MadGraph-5.1.5.12 [34] interfaced with Pythia 8.175 [35] for the decays of the Higgs-boson and the SUSY particles, and for the parton showering and hadronization. The CTEQ6L1 parton distribution functions (PDF) [36] are used. The production cross section of the ggF process is calculated using MCFM [37], while VBFNLO [38] is used for the VBF process. The obtained Higgs-boson production cross section including the signal region jet requirements is 936 ± 50 fb, with 75% of the events from the VBF process and 25% of the events from the ggF process. The BF($h \rightarrow$ NLSP+LSP) is set to 10% when showing representative yields and distributions.

The $Z(\rightarrow \nu\nu)\gamma$, $W(\rightarrow l\nu)\gamma$ and $W(\rightarrow \tau\nu)$ samples are generated using MadGraph-5.1.5.12 and Pythia 8.175. The production of single electroweak bosons is generated using Alpgen-0.0.19 [39] + Jimmy [40] and Sherpa-1.4.0 [41], with up to 5 and 3 additional partons respectively. The Alpgen $W(\rightarrow \mu\nu)$, $W(\rightarrow \tau\nu)$ and $Z(\rightarrow ll)$ samples, and the Sherpa $W(\rightarrow e\nu)$ and $Z(\rightarrow \nu\nu)$ samples, are all normalized to next-to-next-to-leading order (NNLO) cross sections [42]. $W(\rightarrow \tau\nu)$ is a sizable background and high MC statistics is required in the signal region. A MadGraph sample with a generator-level filter is used for the signal region, while an unfiltered Alpgen sample is used for the control regions defined in Sec. 5.2. The diboson samples (WW, WZ, ZZ, $Z(\rightarrow ll)\gamma$) are generated using Sherpa with the CT10 PDF set [43], and are normalized to next-to-leading order (NLO) cross sections [37]. The single-top and $t\bar{t}$ samples are generated using MC@NLO [44]+Jimmy with the CT10 PDF set, and are normalized to NLO cross sections [45]. The process $h \rightarrow \gamma Z$ with $Z \rightarrow \nu\nu$ is not included since the branching fraction of this background is very small [$\sigma_{Higgs} \times$ BF(h $\rightarrow Z\gamma) \times$ BF($Z \rightarrow \nu\nu$) = 936 fb $\times$ 1.6 $\times 10^{-3} \times$ 0.2 = 0.3 fb] [46].

The propagation of particles in the detector is simulated using GEANT4 [47] within the full ATLAS detector simulation [48] for all MC samples except for the signal, $Z(\rightarrow \nu\nu)\gamma$, $W(\rightarrow l\nu)\gamma$ and $W(\rightarrow \tau\nu)$ samples for which fast simulation based on a parametric response of the calorimeters is used [49]. The effect of multiple pp collisions from the same or nearby bunch crossings (in-time or out-of-time pileup) is included in the MC samples by overlaying minimum-bias events onto the hard-scatter events. The MC samples are reconstructed in the same way as the data.

4 Event reconstruction

Photons are reconstructed from energy deposited in clusters of cells in the electromagnetic calorimeter. Photons with $|\eta| < 2.37$ are used. The cluster size is 3×5 cells ($\eta \times \phi$) in the barrel region and 5×5 cells in the end-cap region. The photons for this analysis are required to be *unconverted* [50], having no reconstructed tracks matched to the cluster, to reduce the background from electrons misidentified as photons. The granularity of a cell is 0.025×0.025. Any photon pointing to the transition between the barrel and the end-cap ($1.37 < |\eta| < 1.52$) is not considered.Quality requirements are applied to reject bad quality clusters (clusters with dead cells or cells with distorted signal) or clusters consistent with calorimeter noise. Photons are flagged as bad if they have energy deposited in a narrow $\eta \times \phi$ window or if they are formed from energy deposits that are inconsistent with originating from a pp collision, based on the time of bunch crossing and energy deposition. Identification requirements are made based on shower shapes in the various layers of the electromagnetic calorimeter. Two types of identification are defined, *loose* and *tight* [51]. The tight selection has stronger constraints on the discriminating variables and helps reduce backgrounds from π^0 mesons decaying to photons. The signal photon is required to be tight. The signal photon is also required to pass a *calorimeter isolation* requirement: The transverse energy (E_T^{iso}) in the photon cone with radius ΔR of 0.4 ($\Delta R = \sqrt{(\Delta\eta)^2 + (\Delta\phi)^2} = 0.4$ around the photon cluster), not including the photon cluster, corrected for pileup and energy leakage is required to be less than 5 GeV [52]. The signal photon is also required to be *track isolated*: The ratio of the scalar sum p_T of all tracks in the photon cone with radius 0.2 to the photon p_T is required to be less than 0.05. Signal photons are required to be unconverted and have $p_T > 40$ GeV.

Electrons are also reconstructed from energy clusters in the electromagnetic calorimeter. The same quality criteria applied to photons are applied to electrons. The 'medium' working point defined in Ref. [53, 54] is modified for 2012 data conditions and is used, which requires track-cluster matching and requirements on track hits, along with loose selections on the cluster variables. Electron candidates are required to have $p_T > 7$ GeV and $|\eta| < 2.5$. Muons are reconstructed by combining ID tracks with segments in the MS using the STACO algorithm [55]. Muon candidates are required to have $p_T > 6$ GeV and $|\eta| < 2.5$. Object specific energy scale and resolution corrections and identification efficiency corrections are applied to MC objects based on measurements with data.

Jets are reconstructed from three-dimensional clusters using the anti-k_t algorithm [56] with a radius parameter of 0.4. The clusters are calibrated, weighting differently the energy deposits arising from the electromagnetic and hadronic components of the showers. Area corrections described in Ref. [57] are applied to account for the effects of pileup. Only jets with $p_T > 20$ GeV and $|\eta| < 4.9$ are considered. Quality criteria are applied to jets, and events with bad jets consistent with noise in the calorimeter or non-collision background are vetoed. In order for a jet to be considered for the jet veto (see Sec. 5.2), at least half of the summed p_T of tracks matched to the jet must be associated with tracks originating from the primary vertex (for jet $|\eta| <2.4$), or the jet must have $p_T >50$ GeV. The primary vertex is defined as the vertex with the highest sum of p_T^2 of tracks associated to it. These requirements suppress jets from pileup pp interactions.

Potential ambiguities between reconstructed photons, leptons and jets are resolved by using an overlap removal procedure. The signal photon is identified first, and all objects overlapping with the signal

photon are removed. Jets within the signal photon cone of radius 0.2 are removed. An electron within a jet cone of radius 0.2 is considered to be an electron and the jet is removed. A jet with an electron within an annulus with radius between 0.2 and 0.4 is retained and the electron is removed. A similar annular overlap removal procedure is applied to muons and the remaining jets.

Missing transverse momentum is defined to be the negative vectorial sum of the transverse momenta of the reconstructed electrons, muons, photons, jets and the calorimeter clusters not associated with these objects [58] and its magnitude is denoted by $E_{\mathrm{T}}^{\mathrm{miss}}$. The $E_{\mathrm{T}}^{\mathrm{miss}}$ can be calculated using clusters calibrated at electromagnetic (EM) scale or clusters calibrated individually based on the reconstructed objects they belong to. In this paper $E_{\mathrm{T}}^{\mathrm{miss}}$ refers to the calculation with calorimetric clusters at EM scale, unless otherwise specified. This choice is made to be consistent with the trigger.

5 Event selection

5.1 Triggering

A combined photon plus E_T^{miss} trigger is used to select events. At the EF level, the photon p_T threshold is 40 GeV and the E_T^{miss} threshold is 60 GeV. The trigger selections are the most appropriate for this analysis as the signal is mostly in the region of low photon p_T and E_T^{miss}. A substantial portion of the signal events populate the region where the trigger efficiency is not 100%. The efficiency is measured as a function of the offline photon p_T and E_T^{miss} in data and the measurement is used to correct the trigger simulation.

The trigger efficiency is separately measured for the photon and E_T^{miss} as functions of offline photon p_T and $E_{\mathrm{T}}^{\mathrm{miss}}$, and the two are multiplied to obtain the total trigger efficiency. The photon trigger efficiency is determined as a function of the photon p_T using triggers with lower p_T thresholds [59]. The photon trigger is fully efficient for photon $p_T > 43$ GeV. To study the E_T^{miss} efficiency, the photon cluster selection is replaced with an electron cluster selection, as the difference between a photon and an electron cluster is negligible when calculating the E_T^{miss} at trigger level. The sample is obtained with an electron trigger and is required to have an electron with $p_T > 40$ GeV and at least two jets. It is dominated by $W(\rightarrow e\nu)$+jets events. Corrections are made for other backgrounds (e.g. γ+jets and multijet backgrounds). The E_T^{miss} trigger starts to become efficient for E_T^{miss} of about 50 GeV and becomes fully efficient for E_T^{miss} of about 90 GeV.

5.2 Event selection requirements

The baseline event selection requires events to first pass standard data-quality requirements (accounted for in the calculated integrated luminosity of the data), and pass the combined photon plus E_T^{miss} trigger described in Sec. 5.1. The selected primary vertex must have at least 5 associated tracks. The values of both calibrated and uncalibrated $E_{\mathrm{T}}^{\mathrm{miss}}$ must be greater than 50 GeV. At least one tight isolated photon with $p_T > 40$ GeV is required. Only unconverted photons are used in order to reduce the background from electrons misreconstructed as photons (primarily from W boson decays). If more than one such photon exists in the event, the highest p_T photon is defined to be the signal photon candidate. At least two jets are required with $p_T > 40$ GeV and at least one jet pair must have $m_{jj} > 400$ GeV and $|\Delta\eta_{jj}| > 3.0$, where m_{jj} is the invariant mass of the two jets and $|\Delta\eta_{jj}|$ is the magnitude of the separation of the two jets in η. This is done to loosely select the VBF signature. If more than one pair satisfies these requirements, the pair with the highest invariant mass is considered for further selections described below.

For the signal region, the validation region and most of the control regions, events with a lepton are vetoed in order to reduce electroweak backgrounds. Events are also vetoed if they have more than one selected non-VBF jet with $p_T > 30$ GeV and η in the range spanned by the VBF jets, as the VBF

Table 1: Cutflow for data and GMSB signal (m_{NLSP} , m_{LSP}) = (100, 0) GeV for the signal region as described in Sec. 5.2. Uncertainties are statistical only.

Requirement	Data	(m_{NLSP} , m_{LSP}) = (100, 0) GeV signal
Data quality and trigger	1.53×10^7	337±4
Good vertex	1.53×10^7	336±4
$E_T^{\text{miss}} > 50$ GeV	1.26×10^7	279±3
Selected photon $p_T > 40$ GeV	7.41×10^5	128±2
VBF m_{jj} >400 GeV and $\|\Delta\eta_{jj}\|$ >3.0	3.17×10^4	96.4±1.9
VBF jet $p_T \geq 40$ GeV	6870	58.0±1.5
Lepton veto	6040	57.2±1.5
≤ 1 non-VBF jet	4620	50.4±1.4
$\|\Delta\phi(E_{\text{T}}^{\text{miss}}, VBF\,jet)\|_{min} > 1.4$	600	30.1±1.1
$\|\Delta\phi(E_{\text{T}}^{\text{miss}}, non-VBF\,jet)\|_{min} < 2.0$	565	28.2±1.0
OPV	425	27.6±1.0
$\|\vec{p}_T^{\,TOT}\| \geq 50$ GeV	337	26.9±1.0
$\|\Delta\phi(E_{\text{T}}^{\text{miss}}, \gamma)\| \leq 1.8$	100	21.6±0.9
VBF m_{jj} >600 GeV and $\|\Delta\eta_{jj}\|$ >4.0	50	14.6±0.7

Higgs-boson signal has less QCD radiation between the VBF jets than the background processes. To reduce the background from γ+jets and multijet events, the azimuthal angle between the E_T^{miss} and either of the VBF jets, $|\Delta\phi(E_{\text{T}}^{\text{miss}}, VBF\,jet)|_{min}$ must be >1.4, and the azimuthal angle between the E_T^{miss} and the closest non-VBF jet (if there is one), $|\Delta\phi(E_{\text{T}}^{\text{miss}}, non-VBF\,jet)|_{min}$, must be < 2.0, as described in Sec. 5.2.1.

Following the above requirements, the phase space is divided into regions based on the angle between the photon and E_T^{miss} (see Fig. 2) and the kinematic quantities that distinguish VBF production (m_{jj} and $|\Delta\eta_{jj}|$ shown in Figs. 3 (a) and (b) respectively). These regions are used for the combined γ+jets and multijet background estimation (described in Sec. 6.3).

- Region B : 400 GeV < $m_{jj} \leq 600$ GeV or 3.0 < $|\Delta\eta_{jj}| \leq 4.0$, and $|\Delta\phi(E_{\text{T}}^{\text{miss}}, \gamma)| \leq 1.8$
- Region D : 400 GeV < $m_{jj} \leq 600$ GeV or 3.0 < $|\Delta\eta_{jj}| \leq 4.0$, and $|\Delta\phi(E_{\text{T}}^{\text{miss}}, \gamma)| > 1.8$ (rich in γ+jets and multijet backgrounds)

Lastly, the selected photon is required to be between the VBF jets in η (*outside photon veto* or OPV), and the magnitude of the vector sum p_T of all jets and photons in the event, $|\vec{p}_T^{\,TOT}|$, is required to be > 50 GeV to balance E_T^{miss}. After these two final selections, regions A and C are defined. Region A is the signal region. Table 1 shows the cutflow for data and the GMSB ($m_{\tilde{\chi}^0}$, $m_{\tilde{G}}$) = (100, 0) GeV signal point.

- Region A : $m_{jj} > 600$ GeV, $|\Delta\eta_{jj}| > 4.0$ and $|\Delta\phi(E_{\text{T}}^{\text{miss}}, \gamma)| \leq 1.8$ (signal region)
- Validation region : 400 GeV < $m_{jj} \leq 600$ GeV or 3.0 < $|\Delta\eta_{jj}| \leq 4.0$, and $|\Delta\phi(E_{\text{T}}^{\text{miss}}, \gamma)| \leq 1.8$
- Region C : $m_{jj} > 600$ GeV, $|\Delta\eta_{jj}| > 4.0$ and $|\Delta\phi(E_{\text{T}}^{\text{miss}}, \gamma)| > 1.8$ (rich in γ+jets and multijet backgrounds)

5.2.1 Event selection optimization

Most selection requirements were optimized using the validation region, since this region has similar kinematics to region A but with fewer expected signal events. Each selection requirement was chosen

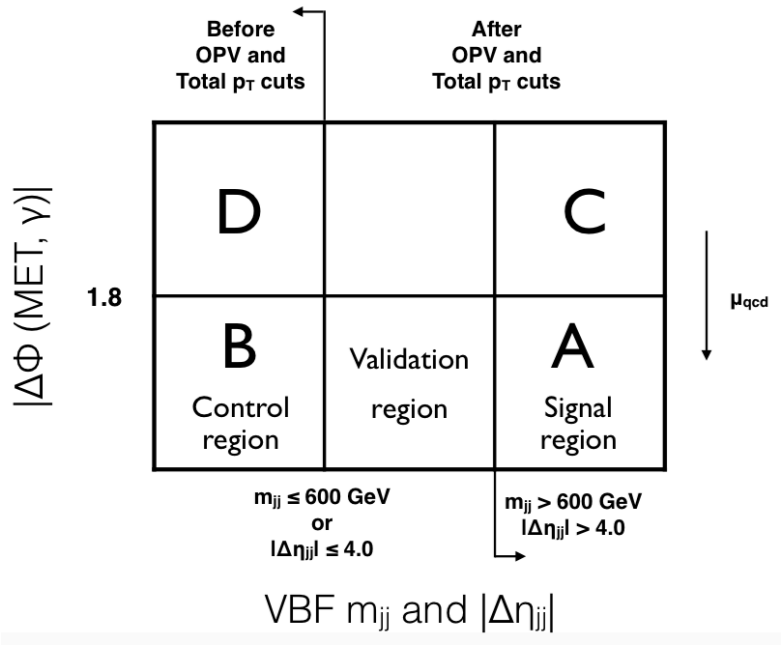

Figure 2: Division of phase space for the combined γ+jets and multijet background estimate.

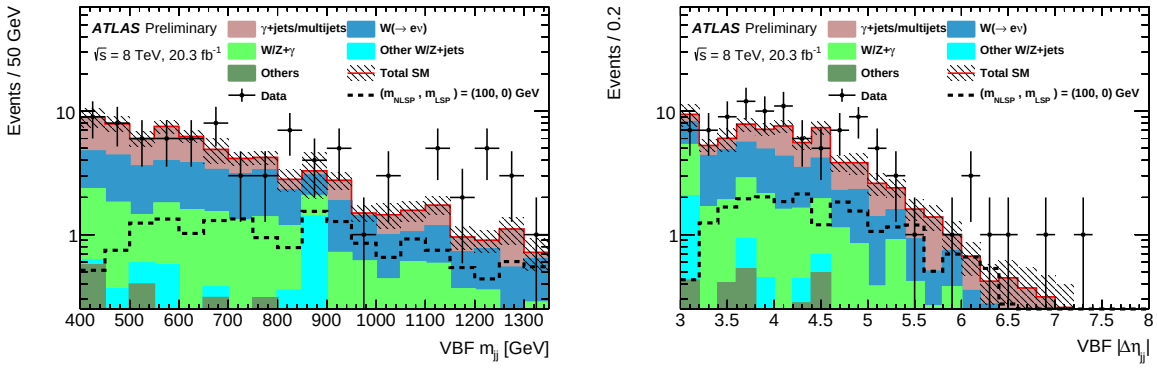

(a) (b)

Figure 3: (a) VBF m_{jj} and (b) VBF $|\Delta\eta_{jj}|$ distributions after all requirements in the combined signal and validation regions. The 'Others' contribution comprises of top and diboson (WW, WZ, ZZ) production. The filled and the hashed regions represent the background yield and the statistical uncertainty on the total background respectively. The black dashed histogram shows the (m_{NLSP} , m_{LSP}) = (100, 0) GeV γ+$E_{\mathrm{T}}^{\mathrm{miss}}$ signal. The shape of the combined γ+jets and multijet background in the signal region are taken from region B, as described in Sec. 6.3. The expected combined γ+jets and multijet background is obtained using the ABCD method as described in Sec. 6.3, assuming no signal in the CR.

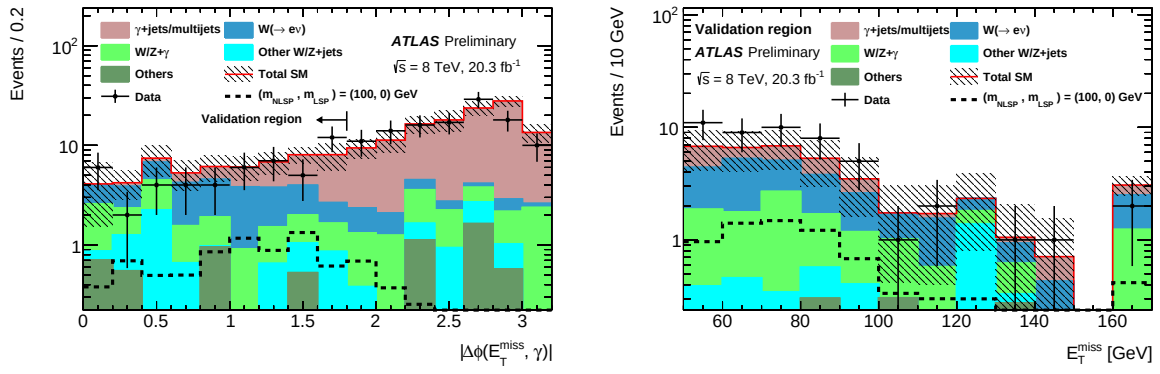

(a) (b)

Figure 4: (a) The $|\Delta\phi(E_{\mathrm{T}}^{\mathrm{miss}},\gamma)|$ distribution with the requirement on it removed and (b) the $E_{\mathrm{T}}^{\mathrm{miss}}$ distribution in the validation region. The 'Others' contribution comprises of top and diboson (WW, WZ, ZZ) production. The filled and the hashed regions represent the background yield and the statistical uncertainty on the total background respectively. The black dashed histogram shows the $(m_{NLSP}, m_{LSP}) = (100, 0)$ GeV γ+$E_{\mathrm{T}}^{\mathrm{miss}}$ signal. The arrow at 1.8 in (a) indicates the requirement on $|\Delta\phi(E_{\mathrm{T}}^{\mathrm{miss}},\gamma)|$ used to define the validation region. The rightmost bin in (b) includes overflow. The expected combined γ+jets and multijet backgrounds in (a) is obtained using the ABCD method as described in Sec. 6.3, assuming no signal in the CR.

to give the highest S/$\sqrt{B}$ in this region, where S (B) is the number of signal (background) events. Figures 4(a) and 4(b) show the $|\Delta\phi(E_{\mathrm{T}}^{\mathrm{miss}},\gamma)|$ and $E_{\mathrm{T}}^{\mathrm{miss}}$ distributions in the validation region. All selection requirements were optimized; a few important requirements are highlighted here.

The electroweak background is almost flat in $|\Delta\phi(E_{\mathrm{T}}^{\mathrm{miss}},\gamma)|$, while the γ+jets and multijet events are mostly in the high $|\Delta\phi(E_{\mathrm{T}}^{\mathrm{miss}},\gamma)|$ region, as shown in Fig. 4 (a). This $E_{\mathrm{T}}^{\mathrm{miss}}$ in γ+jets and multijet events arises from mismeasurement of jets opposite to the photon in azimuth. Figure 4(b) shows the $E_{\mathrm{T}}^{\mathrm{miss}}$ distribution in the validation region. The signal is concentrated at low $E_{\mathrm{T}}^{\mathrm{miss}}$; the $E_{\mathrm{T}}^{\mathrm{miss}}$ threshold is set to 50 GeV to match the trigger threshold.

A selection on $|\Delta\phi(E_{\mathrm{T}}^{\mathrm{miss}}, VBF\,jet)|_{min}$ is applied to remove γ+jets and multijet events. Figure 5(a) shows that most of the γ+jets and multijet events are concentrated at low $|\Delta\phi(E_{\mathrm{T}}^{\mathrm{miss}}, VBF\,jet)|_{min}$, since they have significant $E_{\mathrm{T}}^{\mathrm{miss}}$ due to jet mismeasurement. A requirement of $|\Delta\phi(E_{\mathrm{T}}^{\mathrm{miss}}, VBF\,jet)|_{min} \geq 1.4$ is optimal for the analysis. Figure 5(b) shows the distribution of background events at high $|\Delta\phi(E_{\mathrm{T}}^{\mathrm{miss}}, non-VBF\,jet)|_{min}$ where there is very little signal. The γ+jets and multijet events at high $|\Delta\phi(E_{\mathrm{T}}^{\mathrm{miss}}, non-VBF\,jet)|_{min}$ values are due to a too large measured value of the p_T of a non-VBF jet. The requirement $|\Delta\phi(E_{\mathrm{T}}^{\mathrm{miss}}, non-VBF\,jet)|_{min} \leq 2.0$ is optimal for the analysis. This requirement is fixed in a higher statistics region, obtained by relaxing the requirement $|\Delta\phi(E_{\mathrm{T}}^{\mathrm{miss}}, VBF\,jet)|_{min} \geq 1.4$.

6 Background estimation

The sources of backgrounds are outlined in Table 2 and described in the following sections. Table 3 summarizes the requirements used to define the signal region, the QCD validation region and the various control regions.

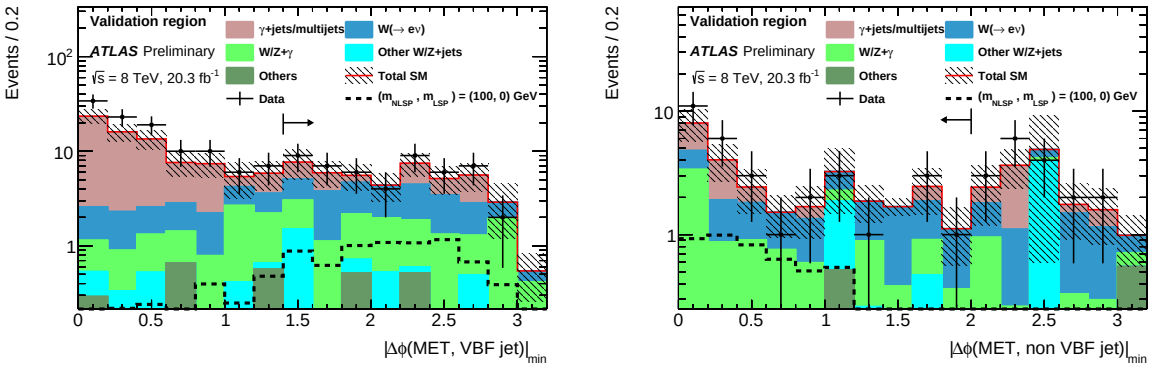

(a) (b)

Figure 5: (a) $|\Delta\phi(E_{\mathrm{T}}^{\mathrm{miss}}, VBF\,jet)|_{min}$ and (b) $|\Delta\phi(E_{\mathrm{T}}^{\mathrm{miss}}, non-VBF\,jet)|_{min}$ distributions in the validation region, with the selection requirement on the plotted variable removed. The 'Others' contribution comprises of top and diboson (WW, WZ, ZZ) production. The filled and the hashed regions represent the background yield and the statistical uncertainty on the total background respectively. The black dashed histogram shows the $(m_{NLSP}, m_{LSP}) = (100, 0)$ GeV γ+$E_{\mathrm{T}}^{\mathrm{miss}}$ signal. The arrows in (a) and (b) indicate the requirements on $|\Delta\phi(E_{\mathrm{T}}^{\mathrm{miss}}, VBF\,jet)|_{min}$ and $|\Delta\phi(E_{\mathrm{T}}^{\mathrm{miss}}, non-VBF\,jet)|_{min}$ respectively to define the validation region.

Table 2: Summary of backgrounds and estimation methods. The dominant backgrounds are normalized to control regions (CR) in data.

Background	Distributions	Normalization
$W(\rightarrow e\nu)$	$W(\rightarrow e\nu)$ MC with $e \rightarrow \gamma$ misidentification rate from data	Data CR
W/Z + jets	W/Z + jets MC with jet$\rightarrow \gamma$ misidentification rate from MC	Data CR
$W\gamma/Z\gamma$	MC	Data CR
Top and diboson	MC	MC
γ + jets and multijet	Data CR	Data CR

6.1 W/Z + jets

The W/Z + jets backgrounds are modeled using a misidentification rate for e$\rightarrow\gamma$ (Sec. 6.1.1), jet$\rightarrow\gamma$ (Sec. 6.1.2), or $\tau\rightarrow\gamma$, and an overall normalization of the MC using $W(\rightarrow e\nu)$ + jets data (Sec. 6.1.3). The total rate for a jet to fake a photon is approximately $(2.5\ \pm\ 0.3)\ \times 10^{-4}$ for hadronic jets, and $(4.2\ \pm\ 1.6)\ \times 10^{-4}$ for jets from τ lepton decays. These rates were derived separately in MC before applying the VBF selection and are not used to obtain the background from jets misidentified as photons. The rate of tight photons in a loose photon sample is used instead, as described in Sec. 6.1.2.

6.1.1 Electrons misidentified as photons: $W(\rightarrow e\nu)$ + jets

The rates of electrons misidentified as photons are derived from data as a function of p_T and $|\eta|$. These rates are applied to electrons in the $W(\rightarrow e\nu)$ + jets MC sample. The sample is normalized to data in the electron control region (see Sec. 6.1.3). The e$\rightarrow\gamma$ misidentification rate is obtained using a tag-and-probe method based on $Z(\rightarrow ee)$ events. Events are selected using an electron trigger, and the tag electron is required to pass tight criteria, to be isolated, and to be matched in ΔR to the electron trigger object that triggered the event. The probe electron/photon is required to be outside the cone of radius 0.4 of the tag electron and the tag-probe system is required to have an invariant mass consistent with the mass of the Z boson (71 GeV $< m_{ee} <$ 101 GeV). The misidentification rate is defined as the ratio of the number of probe photons to the number of probe electrons in the sample. This sample is dominated by $Z\rightarrow ee$ events, and the effect of backgrounds is negligible. The misidentification rate is on average 1% in the barrel region and 2% in the end-cap region.

6.1.2 Jets misidentified as photons: $W(\rightarrow \mu\nu, \tau\nu)$ + jets, $Z(\rightarrow \mu\mu, \tau\tau, \nu\nu)$ + jets

The rate at which a jet is misidentified as a photon is obtained from W/Z+jets MC. Direct photons from the underlying event and final state radiation are modeled with MC and not included in the calculation of the misidentification rate. The misidentification rate is obtained before applying the baseline VBF selection. The rate is measured using a sample with loosely identified photon candidates, and is applied to loosely identified photons in the W/Z+jets MC samples with all other selection requirements applied.

The misidentification rate is calculated and applied separately for jets from quark or gluon hadronization and for jets from τ-lepton decays. A photon candidate within a cone of radius 0.2 from a generated τ lepton is considered to be from the hadronic decay of a τ lepton, while photon candidates outside the τ-lepton cone are assumed to result from other jets. Such a separation is not applied to $W(\rightarrow \mu\nu)$ and $Z(\rightarrow \mu\mu, \nu\nu)$ samples since the misidentified photons are assumed to come from jets and not from a τ lepton decay.

6.1.3 Electron control region

An electron control region is defined to normalize the W/Z+jets MC samples in our signal region. A tight isolated electron is required instead of a signal photon, while keeping all other selections fixed. The selected events are dominated by $W(\rightarrow e\nu)$ + jets events. To estimate the small jet background in this region (< 3% of the total background), the electron identification is loosened while still requiring the electron to be isolated, giving a sample rich in jets misidentified as electrons. A jet-to-electron misidentification factor, defined as the ratio of data after subtracting the EW background contributions in the tight isolated sample to the loose sample, is obtained after requiring the loose VBF selections, $m_{jj} >$ 400 GeV and $|\Delta\eta_{jj}| > 3.0$. This jet-to-electron misidentification factor is used to scale down the loose sample obtained after all event selections for the electron control region, to obtain the jet background contribution.

In order to fix the normalization of W/Z+jets backgrounds using this control region, the jet background and non-$W(\rightarrow e\nu)$+jets backgrounds (estimated from MC) are subtracted from the data. The $W(\rightarrow e\nu)$+jets MC sample is then scaled to match the data in each electron control region. The procedure fixes the $W(\rightarrow e\nu)$+jets MC to the data, and fixes the remaining W/Z+jets normalizations using both the $W(\rightarrow e\nu)$+jets data and the production rates relative to this process. The normalization factors are obtained in a $W(\rightarrow e\nu)$ + $\geq$ 2 jets and are applied to a sample of W/Z + $\geq$ 3 jets where one of the jets fakes a photon. The extrapolation uncertainties are negligible and the other W/Z+jets backgrounds are small. The normalization factors are obtained separately in the signal-like electron control region (e A) and the corresponding regions e C, e D, and e B. These regions are defined with the same selection as regions A, B, C and D, except with the photon replaced by an electron. The normalization factor is 0.90±0.06 for region e A and 0.93±0.05 for e B.

6.2 $W(\rightarrow e\nu, \mu\nu, \tau\nu) + \gamma$ and $Z(\rightarrow \nu\nu, ee, \mu\mu, \tau\tau) + \gamma$

The $W + \gamma$ and $Z(\rightarrow \nu\nu) + \gamma$ background contributions are obtained using a MadGraph $l\nu\gamma$ sample generated in a VBF phase space. The other $Z + \gamma$ background contributions are obtained from Sherpa samples.

A $l\nu\gamma$ data control region is defined to obtain the normalization for $W(\rightarrow l\nu) + \gamma$ events, split into subregions $l\nu\gamma$ A, $l\nu\gamma$ B, $l\nu\gamma$ C, and $l\nu\gamma$ D. It requires events to fail the lepton veto and have a tight, isolated lepton, with all other analysis selections unchanged. The normalization factor of W/Z+jets backgrounds is fixed using the electron control region as described in Sec. 6.1.3.

The non-$W/Z+\gamma$ backgrounds are obtained using MC and subtracted from the data. The normalization factor is obtained by calculating the ratio of this difference to the $W/Z+\gamma$ MC estimate. The regions $l\nu\gamma$ A and $l\nu\gamma$ C (high m_{jj} and $|\Delta\eta_{jj}|$ regions) are combined to obtain the normalization factor for regions A and C. Similarly regions $l\nu\gamma$ B and $l\nu\gamma$ D (lower m_{jj} and $|\Delta\eta_{jj}|$ regions) are combined to obtain the normalization factor for regions B and D. The normalization factors are 1.33±0.42 for regions A+C and 1.17±0.27 for regions B+D.

6.3 γ + jets and multijet

The combined γ+jets and multijet background contribution (including all sources with no significant $E_{\mathrm{T}}^{\mathrm{miss}}$at production) are obtained from data, using an "ABCD" method. The phase space is divided based on the OPV, p_T^{TOT}, m_{jj}, $|\Delta\eta_{jj}|$, and the angle between the photon and E_T^{miss}. Figure 2 illustrates this division. Regions A, B, C and D were defined in Sec. 5.2.

Regions D and C are rich in γ+jets and multijet events, since at large $|\Delta\phi(E_{\mathrm{T}}^{\mathrm{miss}}, \gamma)|$ a missing or under-measured jet can be the source of $E_{\mathrm{T}}^{\mathrm{miss}}$, as shown in Figure 4. The combined γ+jets and multijet contributions in regions D and C are defined as the number of observed data events in each region, after subtracting the number of expected background events from the other sources.

The expected combined γ+jets and multijet events in regions D and C are normalized with the same scale factor μ_{QCD}, to obtain the combined γ+jets and multijet background in regions B and A respectively. The shape of the combined γ+jets and multijet background in the signal region shown in Figures 7(a), 7(b) and 8(b), and is taken from region B. The use of a common scale factor is tested in a γ+jets validation region (VR) defined by inverting the $|\Delta\phi(E_{\mathrm{T}}^{\mathrm{miss}}, VBF\ jet)|_{min}$ requirement while keeping all other cuts fixed. The ratio of the number of events in VR γ+jets B to those in VR γ+jets D is multiplied by the number of events in VR γ+jets C; the result differs from the number of events in VR γ+jets A by a factor of 1.16 ± 0.25; the statistical uncertainty of ± 0.25 from this measurement is taken as the systematic uncertainty for the expected combined γ+jets and multijet background in the signal region. In the statistical fit used to obtain the final result, the combined γ+jet and multijet normalization μ_{QCD} is constrained by the number of observed events in regions B and A and is obtained from a

Table 3: Summary of requirements for various regions. All other analysis requirements are the same for all the regions.

Requirements	Main analysis	Electron CR	$l\nu\gamma$ CR	γ+jets VR
EM object(s)	Photon	Electron	Photon + lepton	Photon
$\lvert\Delta\phi(E_{\mathrm{T}}^{\mathrm{miss}}, VBF\,jet)\rvert_{min}$	> 1.4	> 1.4	> 1.4	≤ 1.4
$m_{jj} \leq 600$ GeV or $\lvert\Delta\eta_{jj}\rvert \leq 4.0$, $\lvert\Delta\phi(E_{\mathrm{T}}^{\mathrm{miss}}, \gamma)\rvert \leq 1.8$	B	e B	$l\nu\gamma$ B	γ+jets B
$m_{jj} > 600$ GeV, $\lvert\Delta\eta_{jj}\rvert > 4.0$, OPV, $p_T^{TOT} \geq 50$ GeV and $\lvert\Delta\phi(E_{\mathrm{T}}^{\mathrm{miss}}, \gamma)\rvert \leq 1.8$	A	e A	$l\nu\gamma$ A	γ+jets A

simultaneous fit of the control and signal region, as described in Sec. 8.

7 Systematic uncertainties

The systematic uncertainties on the background and signal yields are described below and summarized in Table 4.

The electron control region is used to obtain the normalization factors for the W/Z+jet backgrounds in each of the four regions A, B, C and D; resulting in an uncertainty of 6% on the W/Z+jet background yield in the signal region. The $l\nu\gamma$ control regions are used to obtain the normalization factors for the $W/Z+\gamma$ background; resulting in an uncertainty of 31% on the $W/Z+\gamma$ background yield in the signal region. The statistical uncertainty on the $e \to \gamma$ misidentification rate leads to a 5% uncertainty on the $W(\to e\nu)$ background in the signal region. The electroweak backgrounds due to jets faking photons are very small and determined from MC. An uncertainty of 100% is assigned on the probability for a simulated jet to be misidentified as a selected photon, based on a study comparing data to MC photon identification and isolation fake rates in the electron control region with loose cuts after the VBF baseline selection. An uncertainty of 100% is assigned to the $W(\to \mu\nu)$ and $W(\to \tau\nu)$ backgrounds when the photon comes from the underlying event. This leads to an uncertainty of 0.2 events and 0.17 events on the $W(\to \mu\nu)$ and $W(\to \tau\nu)$ background estimates respectively. The relative uncertainties on Z+jets and $W(\to \mu\nu)$ background yields are greater than 100%, but the absolute uncertainties on these backgrounds are much smaller than the total expected background.

Since the combined γ+jets and multijet background is obtained from a fit to the data with the electroweak backgrounds subtracted, the normalization uncertainty on these backgrounds leads to an (anti-correlated) uncertainty on the combined γ+jets and multijet background estimate. There is also a systematic uncertainty on the combined γ+jets and multijet background in the signal region due to the assumption that the combined γ+jets and multijet background scales the same way in region AC as in region BD. This uncertainty is 25% on the estimate in the signal region, as found from the QCD validation region (Sec. 6.3).

The photon trigger efficiency uncertainty is negligible. The $E_{\mathrm{T}}^{\mathrm{miss}}$ trigger efficiency is obtained from data and MC by studying $W(\to e\nu)$+jets events with an electron having $p_T > 40$ GeV, and at least two jets. The efficiency curves are also studied using events with other topologies. Events with (a) no jets, (b) two jets satisfying the VBF topology and (c) transverse mass of the electron - $E_{\mathrm{T}}^{\mathrm{miss}}$ system, $m_T \geq 50$ GeV, are used to obtain separate efficiency curves. The final yield is compared using the different efficiency curves, leading to an uncertainty on the signal efficiency of $< 2\%$. This uncertainty is applied to all signal models considered.

The uncertainty on both the jet energy resolution and the jet energy scale [60] leads to an uncertainty of 4% and 7% respectively on the signal efficiency. The uncertainty on both the photon energy scale and photon energy resolution leads to an uncertainty of 1% respectively on the signal efficiency.

Table 4: Summary of the systematic uncertainties on the number of events for the (m_{NLSP} , m_{LSP}) = (100, 0) GeV γ+$E_{\mathrm{T}}^{\mathrm{miss}}$ signal and background in the signal region. The 'Others' background consists of top and diboson (WW, WZ, ZZ) production. The last column shows the breakdown of the systematics on the signal yield in the signal region. The total uncertainty is calculated by adding all the uncertainties in quadrature. Correlations between the control and signal regions are not taken into account in the calculation of the total uncertainty shown here.

Systematic	$Z(\to \nu\nu)\gamma$	$W(\to l\nu)\gamma$	$Z(\to \nu\nu)$	$Z(\to \tau\tau)$	$W(\to e\nu)$	$W(\to \mu\nu)$	$W(\to \tau\nu)$	Others	γ+jets	Signal
W/Z+jets norm.	0	0	0.02	0.01	0.64	0.01	0.25	0	0.28	0
W/Z+γ norm.	0.19	2.2	0	0	0	0	0	0	0.28	0
$e \to \gamma$ misid. rate	0	0	0	0	0.54	0	0	0	0	0
jet$\to \gamma$ misid. rate	0	0	0.28	0.24	0	0.01	0.42	0	0	0
MC γ rate	0	0	0	0	0	0.2	0.17	0	0	0
Trigger efficiency	0.01	0.14	0.01	0	0.21	0	0.08	0.01	0	0.29
ABCD	0	0	0	0	0	0	0	0	3.5	0
Jet energy resolution	0.03	0.22	0.28	0	0.43	0.09	0.18	0.14	0.28	0.58
Jet energy scale	0.02	0.5	0.28	0.02	1.2	0.08	0.17	0.22	0.14	1.0
γ energy resolution	0.01	0.07	0	0	0	0	0.19	0	0	0.15
γ energy scale	0.02	0.22	0.01	0	0	0	0.19	0	0	0.15
Cross section	0	0	0	0	0	0	0	0	0	0.8
Total	0.2	2.3	0.48	0.24	1.5	0.24	0.65	0.26	3.5	1.2

The signal production is divided into ggF and VBF production channels. The uncertainties on the NLO normalization factors result in an uncertainty of 42 fb on the ggF cross section, and an uncertainty of 33 fb on the VBF cross section, leading to an uncertainty of 50 fb (5.3%) on the total cross section. These normalization factor uncertainties were obtained by changing the renormalization and factorization scales by a factor of ±2.

8 Results and interpretation

The expected number of signal events in the signal region, assuming BF($h \to$ NLSP + LSP) = 10%, is shown in Figure 6. The distributions of m_T, γ p_T, $|\Delta\phi(E_{\mathrm{T}}^{\mathrm{miss}}, \gamma)|$ and $E_{\mathrm{T}}^{\mathrm{miss}}$ are shown in Figures. 7–8 after applying all signal region selections and background normalization factors; m_T is defined as $m_T = \sqrt{2\, E_T^{\gamma}\, E_{\mathrm{T}}^{\mathrm{miss}}[1 - \cos\Delta\phi(E_{\mathrm{T}}^{\mathrm{miss}}, \gamma)]}$. The combined γ+jets and multijet distribution in the signal region is taken from the γ+jets validation region and scaled to the expected combined γ+jets and multijet background yield in the signal region. The distributions are not used in setting limits, only the numbers of events. In particular, the number of selected photons and other distributions based on a second-leading-p_T photon, are not used for the search. Table 5 shows the expected number of background and signal events, as well as the observed data events, in the signal region and the various control regions. The combined γ+jets and multijet yields in γ+jets A and region B are defined as the number of observed data events in γ+jets A and region B, after subtracting EW background events in the respective regions. Thus the total background agrees with data in γ+jets A and region B by construction. The expected background events in e A and $l\nu\gamma$ A are shown before applying the obtained normalization factors. A simultaneous fit to the regions B and A is used to derive the combined γ+jets and multijet background and signal yields. The combined γ+jets and multijets background and signal in regions B and A are both included in the fit and constrained by the number of observed events in the two regions. Table 6 shows the results of the signal+background fit for the reference signal point, (m_{NLSP} , m_{LSP}) = (100, 0) GeV. The best fit value of the signal yield corresponds to a BF of 11.6% ± 10.9%. Table 7 shows the results of the background-only fit in the combined CR+SR. The significance of the excess of observed data over the expected SM backgrounds is 1.1σ. The combined γ+jets and multijet background is higher after the

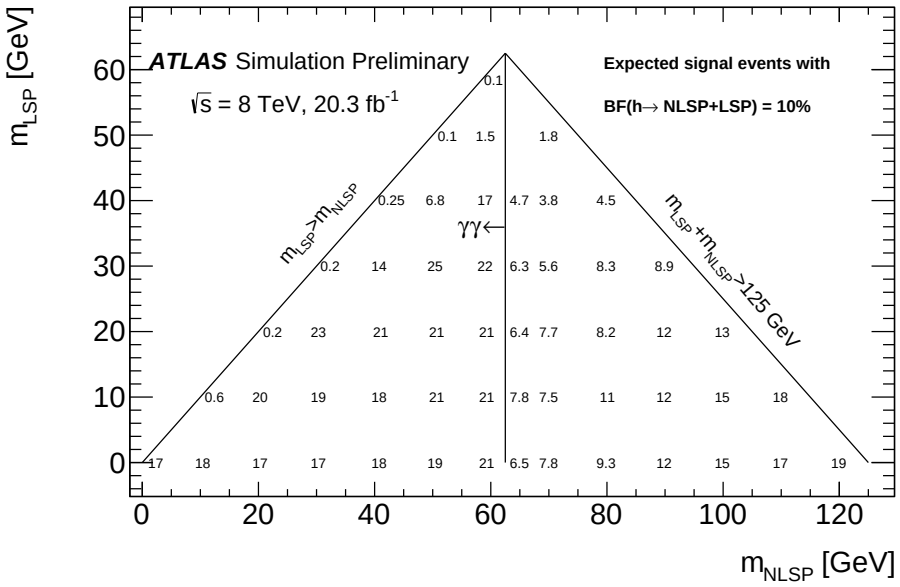

Figure 6: Expected number of signal events (assuming BF($h \rightarrow$ NLSP+LSP) = 10%) in the signal region for different NLSP and LSP masses. The vertical line separates signal final states of $\gamma\gamma$+$E_{\mathrm{T}}^{\mathrm{miss}}$ (left) from γ+$E_{\mathrm{T}}^{\mathrm{miss}}$ (right).

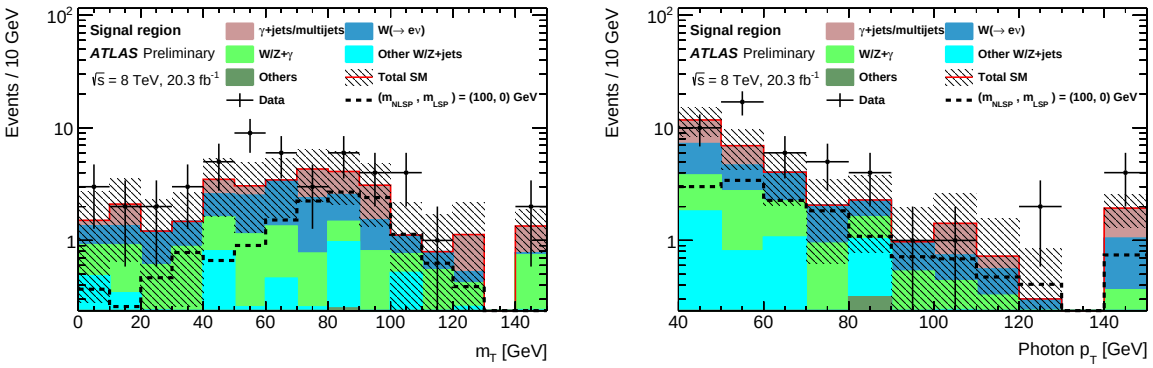

(a) (b)

Figure 7: (a) Transverse mass (m_T) and (b) photon p_T distributions in the signal region. The 'Others' contribution comprises of top and diboson (WW, WZ, ZZ) production. The filled and the hashed regions represent the background yield and the statistical uncertainty on the total background respectively. The black dashed histogram shows the (m_{NLSP} , m_{LSP}) = (100, 0) GeV γ+$E_{\mathrm{T}}^{\mathrm{miss}}$ signal. The rightmost bin in (a) and (b) includes overflow.

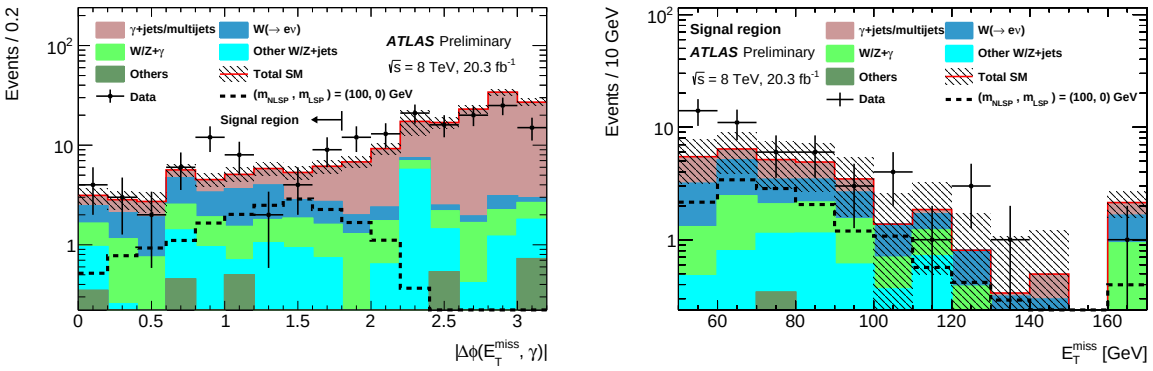

(a) (b)

Figure 8: (a) The $|\Delta\phi(E_{\mathrm{T}}^{\mathrm{miss}}, \gamma)|$ distribution in regions A and C, and (b) $E_{\mathrm{T}}^{\mathrm{miss}}$ distribution in the signal region. The 'Others' contribution comprises of top and diboson (WW, WZ, ZZ) production. The filled and hashed regions represent the background yield and the statistical uncertainty on the total background respectively. The black dashed histogram shows the (m_{NLSP}, m_{LSP}) = (100, 0) GeV γ+$E_{\mathrm{T}}^{\mathrm{miss}}$ signal. The arrow at 1.8 in (a) indicates the requirement on $|\Delta\phi(E_{\mathrm{T}}^{\mathrm{miss}}, \gamma)|$ used to define the signal region. The rightmost bin in (b) includes overflow.

Table 5: Summary of expected background and signal yields, along with the statistical and systematic uncertainties, in various control and signal regions. The expected combined γ+jets and multijet background is obtained using the ABCD method as described in Sec. 6.3, assuming no signal in the CR. The 'Others' background consists of top and diboson (WW, WZ, ZZ) production. The systematic uncertainties are obtained by adding the various uncertainties in quadrature. Correlations between the control and signal regions are not taken into account in the calculation of the total uncertainty shown here.

	SR	Region B	γ+jets A	e A	$l\nu\gamma$ A
$W(\rightarrow e\nu)$	10.7 ± 0.7 ± 1.5	24.5 ± 1.0 ± 3.3	5.2 ± 0.4 ± 0.6	956 ± 53 ± 133	0.02 ± 0.01 ± 0.00
$W(\rightarrow \mu\nu)$	0.21 ± 0.1 ± 0.24	1.4 ± 1.3 ± 0.3	0.1 ± 0.06 ± 0.06	0	0.66 ± 0.17 ± 0.09
$W(\rightarrow \tau\nu)$	4.2 ± 0.8 ± 0.6	4.7 ± 2.6 ± 2.4	1.7 ± 0.6 ± 0.8	62 ± 3.4 ± 37	0.9 ± 0.5 ± 0.33
$W(\rightarrow l\nu)\gamma$	7.2 ± 0.5 ± 2.3	11.9 ± 0.6 ± 4.1	3.6 ± 0.3 ± 1.2	4.0 ± 0.3 ± 0.2	6.0 ± 0.4 ± 0.4
Z+jets	0.52 ± 0.28 ± 0.54	3.7 ± 3.5 ± 3.5	0	12.3 ± 7.1 ± 2.9	0
$Z+\gamma$	0.61 ± 0.05 ± 0.2	2.6 ± 1.4 ± 1.4	1.1 ± 0.8 ± 0.8	0	0.37 ± 0.37 ± 0.09
Others	0.68 ± 0.4 ± 0.26	2.6 ± 0.8 ± 0.6	0.8 ± 0.4 ± 0.6	99.8 ± 5.1 ± 4.0	2.0 ± 0.7 ± 0.8
γ+jets and multijet	13.9 ± 1.7 ± 3.5	26.6 ± 2.2 ± 0.8	31.5 ± 6.7 ± 2.0	37 ± 11 ± 36	0
Total background	38.0 ± 2.2 ± 4.5	78 ± 5.4 ± 7	44 ± 6.8 ± 2.8	1170 ± 55 ± 143	10.0 ± 1 ± 0.9
Data	50	78	44	1079	12
(m_{NLSP}, m_{LSP}) (100, 0) GeV	14.6 ± 0.7 ± 1.2	8.5 ± 0.6 ± 0.6	3.0 ± 0.3 ± 0.5	0.3 ± 0.1 ± 0.1	0.11 ± 0.06 ± 0.07

	Control region	Signal region
Observed events	78	50
Fitted events	78.0 ± 7.4	50.0 ± 8.1
Fitted $Z(\to \nu\nu)\gamma$ events	0.71 ± 0.2	0.62 ± 0.21
Fitted $Z(\to \tau\tau)\gamma$ events	1.9 ± 1.2	0.0 ± 0.0
Fitted $W(\to l\nu)\gamma$ events	11.9 ± 4.2	7.2 ± 2.4
Fitted $Z(\to \nu\nu)$ events	0.02 ± 0.01	$0.28^{+0.49}_{-0.28}$
Fitted $Z(\to \tau\tau)$ events	3.6 ± 3.4	$0.24^{+0.24}_{-0.24}$
Fitted $W(\to e\nu)$ events	24.5 ± 3.7	10.7 ± 1.8
Fitted $W(\to \mu\nu)$ events	1.4 ± 0.2	$0.21^{+0.24}_{-0.21}$
Fitted $W(\to \tau\nu)$ events	4.7 ± 2.4	4.2 ± 0.8
Fitted Others events	2.6 ± 0.6	0.68 ± 0.27
Fitted γ+jets and multijet events	$16.8^{+17.6}_{-16.8}$	$8.8^{+10.0}_{-8.8}$
Fitted $(m_{NLSP}, m_{LSP}) = (100, 0)$ GeV events	9.9 ± 9.7	17.0 ± 15.9

Table 6: Signal+background fit of regions B and A for $(m_{NLSP}, m_{LSP}) = (100, 0)$ GeV signal showing the best fit values and uncertainties for the background and signal events. The 'Others' background consists of top and diboson (WW, WZ, ZZ) production. The fit includes the correlation of uncertainties between the control and signal regions.

fit than the expectation in the SR as seen in Table 5, because of the excess of observed data in the SR.

Figure 9 and Table 8 show the expected and observed limits on the $(\sigma/\sigma_{SM})\times BF(h \to \text{NLSP+LSP})$ at 95% confidence level (CL) for the monophoton and and diphoton signal samples, obtained using the CL_s method [61] with an Asimov approximation, implemented in HistFitter [62]. The $\pm 1\sigma$ and $\pm 2\sigma$ excursions of the expected limit in absence of signal are shown for all model parameters considered. The observed limit is higher than the expected limit for all signal points since the number of events observed in the signal region (50) is larger than the number of events expected from background processes (38). For instance the observed limit on $(\sigma/\sigma_{SM})\times BF(h \to \text{NLSP+LSP})$ for the reference signal $(m_{NLSP}, m_{LSP}) = (100, 0)$ GeV (0.33) seen in Table 8, is approximately 2σ higher than the best fit value (0.12 ± 0.11) which corresponds to the best fit signal yield (17.0 ± 15.9 events) seen in Table 6. Figure 10 shows the observed limits for different NLSP and LSP masses. Although the analysis was optimized for a γ+$E_{\mathrm{T}}^{\mathrm{miss}}$ search, strong upper limits are obtained on the branching fraction of the Higgs-boson to NLSP+LSP particles leading to a $\gamma\gamma$+$E_{\mathrm{T}}^{\mathrm{miss}}$ final state.

9 Conclusion

A search has been performed for Higgs-boson decays to neutralinos and gravitinos, using VBF Higgs-boson production and a final-state signature of at least one photon, $E_{\mathrm{T}}^{\mathrm{miss}}$, and two VBF jets. The full 2012 8 TeV pp dataset from the ATLAS detector at the LHC was studied, corresponding to an integrated luminosity of 20.3 fb^{-1} . The search was optimized for $h \to \tilde{\chi}^0\tilde{G} \to \gamma\,\tilde{G}\,\tilde{G}$ signal leading to a $\gamma + E_{\mathrm{T}}^{\mathrm{miss}}+ jj$ final state, and also applied to models with $h \to \tilde{\chi}_2^0\tilde{\chi}_1^0 \to \gamma\,\tilde{\chi}_1^0\,\tilde{\chi}_1^0$ leading to a $\gamma + E_{\mathrm{T}}^{\mathrm{miss}}+ jj$ final state, and $h \to \tilde{\chi}_2^0\tilde{\chi}_2^0 \to \gamma\,\gamma\,\tilde{\chi}_1^0\,\tilde{\chi}_1^0$ leading to a $\gamma\gamma + E_{\mathrm{T}}^{\mathrm{miss}}+ jj$ final state. After all selections, the number of events observed agree with the SM backgrounds within uncertainties. The limits obtained are similar to or stronger than indirect limits from the Higgs-boson coupling measurements, and are the first direct limits on these Higgs-boson decays.

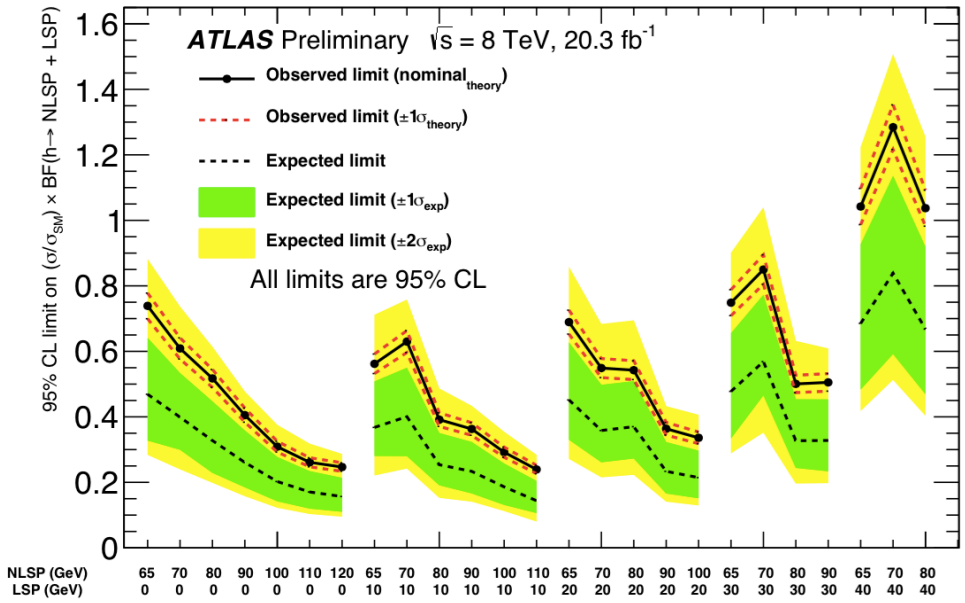

(a)

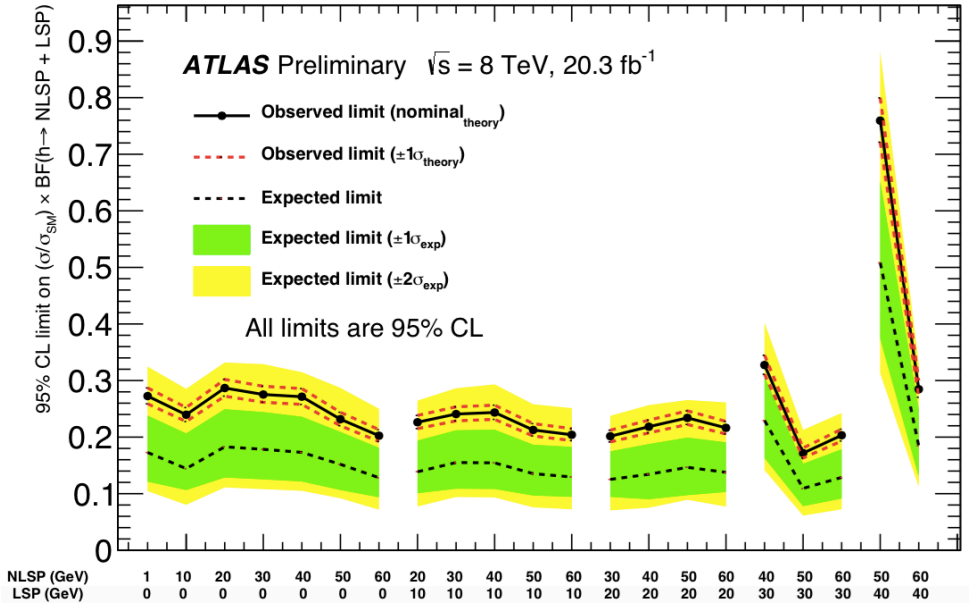

(b)

Figure 9: Observed and expected limits for various NLSP and LSP masses for (a) monophoton signals and (b) diphoton signals. The green and yellow bands show the $\pm 1\sigma$ and $\pm 2\sigma$ excursions of the expected limits respectively

	Control region	Signal region
Observed events	78	50
Fitted events	79.6 ± 7.2	43.2 ± 4.4
Fitted $Z(\to \nu\nu)\gamma$ events	0.72 ± 0.16	0.74 ± 0.19
Fitted $Z(\to \tau\tau)\gamma$ events	2.0 ± 0.9	0.0 ± 0.0
Fitted $W(\to l\nu)\gamma$ events	11.9 ± 3.0	8.6 ± 2.2
Fitted $Z(\to \nu\nu)$ events	0.02 ± 0.01	$0.25^{+0.44}_{-0.25}$
Fitted $Z(\to \tau\tau)$ events	4.2 ± 2.7	0.28 ± 0.24
Fitted $W(\to e\nu)$ events	24.9 ± 2.7	11.4 ± 1.3
Fitted $W(\to \mu\nu)$ events	1.5 ± 0.2	$0.25^{+0.26}_{-0.25}$
Fitted $W(\to \tau\nu)$ events	5.1 ± 2.2	4.5 ± 0.6
Fitted Others events	2.7 ± 0.5	0.75 ± 0.21
Fitted γ+jets and multijet events	26.5 ± 1.8	16.4 ± 3.4

Table 7: Background-only fit of regions B and A showing the best fit values and uncertainties for the background events. The 'Others' background consists of top and diboson (WW, WZ, ZZ) production. The fit includes the correlation of uncertainties between the control and signal regions.

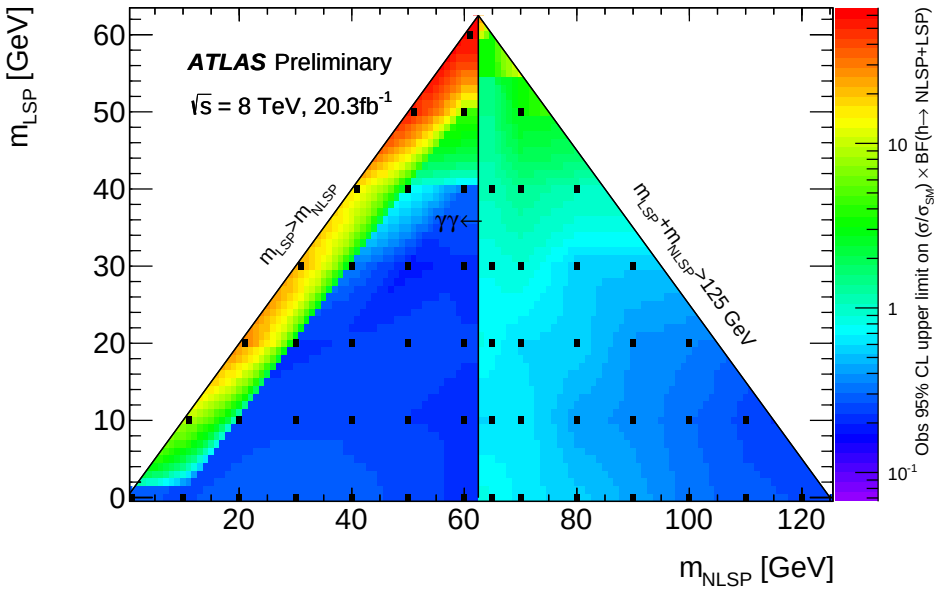

Figure 10: Observed limits for various NLSP and LSP masses. The black squares indicate the generated signal points that are used for interpolation.

Signal	m_{NLSP} (GeV)	m_{LSP} (GeV)	95% CL Obs.	95% CL Exp.$^{+1\sigma}_{-1\sigma}$
$\gamma+E_{\mathrm{T}}^{\mathrm{miss}}$	65	0	0.78	$0.47^{+0.17}_{-0.14}$
$\gamma+E_{\mathrm{T}}^{\mathrm{miss}}$	70	0	0.64	$0.40^{+0.13}_{-0.10}$
$\gamma+E_{\mathrm{T}}^{\mathrm{miss}}$	80	0	0.54	$0.33^{+0.12}_{-0.10}$
$\gamma+E_{\mathrm{T}}^{\mathrm{miss}}$	90	0	0.43	$0.26^{+0.10}_{-0.08}$
$\gamma+E_{\mathrm{T}}^{\mathrm{miss}}$	100	0	0.33	$0.20^{+0.07}_{-0.06}$
$\gamma+E_{\mathrm{T}}^{\mathrm{miss}}$	110	0	0.28	$0.17^{+0.06}_{-0.05}$
$\gamma+E_{\mathrm{T}}^{\mathrm{miss}}$	120	0	0.26	$0.16^{+0.06}_{-0.05}$
$\gamma+E_{\mathrm{T}}^{\mathrm{miss}}$	65	10	0.59	$0.37^{+0.14}_{-0.09}$
$\gamma+E_{\mathrm{T}}^{\mathrm{miss}}$	70	10	0.66	$0.40^{+0.15}_{-0.12}$
$\gamma+E_{\mathrm{T}}^{\mathrm{miss}}$	80	10	0.41	$0.25^{+0.10}_{-0.06}$
$\gamma+E_{\mathrm{T}}^{\mathrm{miss}}$	90	10	0.38	$0.23^{+0.09}_{-0.07}$
$\gamma+E_{\mathrm{T}}^{\mathrm{miss}}$	100	10	0.31	$0.19^{+0.07}_{-0.06}$
$\gamma+E_{\mathrm{T}}^{\mathrm{miss}}$	110	10	0.25	$0.14^{+0.06}_{-0.04}$
$\gamma+E_{\mathrm{T}}^{\mathrm{miss}}$	65	20	0.73	$0.45^{+0.18}_{-0.12}$
$\gamma+E_{\mathrm{T}}^{\mathrm{miss}}$	70	20	0.58	$0.36^{+0.14}_{-0.10}$
$\gamma+E_{\mathrm{T}}^{\mathrm{miss}}$	80	20	0.57	$0.37^{+0.14}_{-0.10}$
$\gamma+E_{\mathrm{T}}^{\mathrm{miss}}$	90	20	0.38	$0.23^{+0.09}_{-0.07}$
$\gamma+E_{\mathrm{T}}^{\mathrm{miss}}$	100	20	0.35	$0.21^{+0.08}_{-0.06}$
$\gamma+E_{\mathrm{T}}^{\mathrm{miss}}$	65	30	0.79	$0.48^{+0.18}_{-0.14}$
$\gamma+E_{\mathrm{T}}^{\mathrm{miss}}$	70	30	0.89	$0.57^{+0.20}_{-0.10}$
$\gamma+E_{\mathrm{T}}^{\mathrm{miss}}$	80	30	0.53	$0.33^{+0.13}_{-0.08}$
$\gamma+E_{\mathrm{T}}^{\mathrm{miss}}$	90	30	0.53	$0.33^{+0.13}_{-0.09}$
$\gamma+E_{\mathrm{T}}^{\mathrm{miss}}$	65	40	1.10	$0.69^{+0.24}_{-0.20}$
$\gamma+E_{\mathrm{T}}^{\mathrm{miss}}$	70	40	1.35	$0.84^{+0.30}_{-0.25}$
$\gamma+E_{\mathrm{T}}^{\mathrm{miss}}$	80	40	1.09	$0.67^{+0.25}_{-0.20}$
$\gamma+E_{\mathrm{T}}^{\mathrm{miss}}$	70	50	2.82	$1.73^{+0.65}_{-0.51}$
$\gamma\gamma+E_{\mathrm{T}}^{\mathrm{miss}}$	1	0	0.29	$0.17^{+0.07}_{-0.05}$
$\gamma\gamma+E_{\mathrm{T}}^{\mathrm{miss}}$	10	0	0.25	$0.14^{+0.06}_{-0.04}$
$\gamma\gamma+E_{\mathrm{T}}^{\mathrm{miss}}$	20	0	0.30	$0.18^{+0.07}_{-0.05}$
$\gamma\gamma+E_{\mathrm{T}}^{\mathrm{miss}}$	30	0	0.29	$0.18^{+0.07}_{-0.05}$
$\gamma\gamma+E_{\mathrm{T}}^{\mathrm{miss}}$	40	0	0.29	$0.17^{+0.06}_{-0.05}$
$\gamma\gamma+E_{\mathrm{T}}^{\mathrm{miss}}$	50	0	0.24	$0.15^{+0.06}_{-0.05}$
$\gamma\gamma+E_{\mathrm{T}}^{\mathrm{miss}}$	60	0	0.21	$0.13^{+0.05}_{-0.03}$
$\gamma\gamma+E_{\mathrm{T}}^{\mathrm{miss}}$	11	10	8.69	$5.56^{+1.82}_{-1.58}$
$\gamma\gamma+E_{\mathrm{T}}^{\mathrm{miss}}$	20	10	0.24	$0.14^{+0.06}_{-0.04}$
$\gamma\gamma+E_{\mathrm{T}}^{\mathrm{miss}}$	30	10	0.25	$0.16^{+0.06}_{-0.05}$
$\gamma\gamma+E_{\mathrm{T}}^{\mathrm{miss}}$	40	10	0.26	$0.15^{+0.06}_{-0.05}$
$\gamma\gamma+E_{\mathrm{T}}^{\mathrm{miss}}$	50	10	0.22	$0.14^{+0.05}_{-0.04}$
$\gamma\gamma+E_{\mathrm{T}}^{\mathrm{miss}}$	60	10	0.21	$0.13^{+0.05}_{-0.04}$
$\gamma\gamma+E_{\mathrm{T}}^{\mathrm{miss}}$	21	20	28.48	$17.47^{+6.77}_{-3.89}$
$\gamma\gamma+E_{\mathrm{T}}^{\mathrm{miss}}$	30	20	0.21	$0.13^{+0.05}_{-0.04}$
$\gamma\gamma+E_{\mathrm{T}}^{\mathrm{miss}}$	40	20	0.23	$0.13^{+0.05}_{-0.04}$
$\gamma\gamma+E_{\mathrm{T}}^{\mathrm{miss}}$	50	20	0.25	$0.15^{+0.05}_{-0.04}$
$\gamma\gamma+E_{\mathrm{T}}^{\mathrm{miss}}$	60	20	0.23	$0.14^{+0.05}_{-0.04}$
$\gamma\gamma+E_{\mathrm{T}}^{\mathrm{miss}}$	31	30	21.87	$14.10^{+4.63}_{-3.84}$
$\gamma\gamma+E_{\mathrm{T}}^{\mathrm{miss}}$	40	30	0.34	$0.23^{+0.08}_{-0.07}$
$\gamma\gamma+E_{\mathrm{T}}^{\mathrm{miss}}$	50	30	0.18	$0.11^{+0.04}_{-0.03}$
$\gamma\gamma+E_{\mathrm{T}}^{\mathrm{miss}}$	60	30	0.21	$0.13^{+0.05}_{-0.04}$
$\gamma\gamma+E_{\mathrm{T}}^{\mathrm{miss}}$	41	40	15.44	$9.73^{+3.85}_{-2.47}$
$\gamma\gamma+E_{\mathrm{T}}^{\mathrm{miss}}$	50	40	0.80	$0.51^{+0.14}_{-0.13}$
$\gamma\gamma+E_{\mathrm{T}}^{\mathrm{miss}}$	60	40	0.30	$0.18^{+0.06}_{-0.05}$
$\gamma\gamma+E_{\mathrm{T}}^{\mathrm{miss}}$	51	50	51.26	$37.64^{+8.95}_{-6.64}$
$\gamma\gamma+E_{\mathrm{T}}^{\mathrm{miss}}$	60	50	4.26	$2.30^{+0.59}_{-0.44}$
$\gamma\gamma+E_{\mathrm{T}}^{\mathrm{miss}}$	61	60	60.67	$37.71^{+14.36}_{-10.50}$

Table 8: 95% CL observed and expected limits on $(\sigma/\sigma_{SM}) \times BF(h \to NLSP + LSP)$ for all the signal points. The $\pm 1\ \sigma$ excursions of the expected limit are also shown for all the signal points.

References

[1] ATLAS Collaboration, *Observation of a new particle in the search for the Standard Model Higgs boson with the ATLAS detector at the LHC*, Phys.Lett. **B716** (2012) 1–29, arXiv:1207.7214 [hep-ex].

[2] CMS Collaboration, *Observation of a new boson at a mass of 125 GeV with the CMS experiment at the LHC*, Phys.Lett. **B716** (2012) 30–61, arXiv:1207.7235 [hep-ex].

[3] ATLAS Collaboration, *Combined coupling measurements of the Higgs-like boson with the ATLAS detector using up to 25 fb^{-1} of proton-proton collision data*, ATLAS-CONF-2013-034 (2013). https://cds.cern.ch/record/1528170.

[4] D. Curtin, R. Essig, S. Gori, P. Jaiswal, A. Katz, et al., *Exotic Decays of the 125 GeV Higgs Boson*, arXiv:1312.4992 [hep-ph].

[5] H. Miyazawa, *Baryon Number Changing Currents*, Prog. Theor. Phys. **36 (6)** (1966) 1266–1276.

[6] P. Ramond, *Dual Theory for Free Fermions*, Phys. Rev. **D3** (1971) 2415–2418.

[7] Y. A. Gol'fand and E. P. Likhtman, *Extension of the Algebra of Poincare Group Generators and Violation of p Invariance*, JETP Lett. **13** (1971) 323–326. [PismaZh.Eksp.Teor.Fiz.13:452-455,1971].

[8] A. Neveu and J. H. Schwarz, *Factorizable dual model of pions*, Nucl. Phys. **B31** (1971) 86–112.

[9] A. Neveu and J. H. Schwarz, *Quark Model of Dual Pions*, Phys. Rev. **D4** (1971) 1109–1111.

[10] J. Gervais and B. Sakita, *Field theory interpretation of supergauges in dual models*, Nucl. Phys. **B34** (1971) 632–639.

[11] D. V. Volkov and V. P. Akulov, *Is the Neutrino a Goldstone Particle?*, Phys. Lett. **B46** (1973) 109–110.

[12] J. Wess and B. Zumino, *A Lagrangian Model Invariant Under Supergauge Transformations*, Phys. Lett. **B49** (1974) 52.

[13] J. Wess and B. Zumino, *Supergauge Transformations in Four-Dimensions*, Nucl. Phys. **B70** (1974) 39–50.

[14] S. Dimopoulos and H. Georgi, *Softly Broken Supersymmetry and SU(5)*, Nucl. Phys. **B193** (1981) 150.

[15] E. Witten, *Dynamical Breaking of Supersymmetry*, Nucl. Phys. **B188** (1981) 513.

[16] M. Dine, W. Fischler, and M. Srednicki, *Supersymmetric Technicolor*, Nucl. Phys. **B189** (1981) 575–593.

[17] S. Dimopoulos and S. Raby, *Supercolor*, Nucl. Phys. **B192** (1981) 353.

[18] N. Sakai, *Naturalness in Supersymmetric Guts*, Zeit. Phys. **C11** (1981) 153.

[19] R. K. Kaul and P. Majumdar, *Cancellation of quadratically divergent mass corrections in globally supersymmetric spontaneously broken gauge theories*, Nuclear Physics B **199** no. 1, (1982) 36 – 58.

[20] M. Dine and W. Fischler, *A Phenomenological Model of Particle Physics Based on Supersymmetry*, Phys. Lett. **B110** (1982) 227.

[21] L. Alvarez-Gaume, M. Claudson, and M. B. Wise, *Low-Energy Supersymmetry*, Nucl. Phys. **B207** (1982) 96.

[22] C. R. Nappi and B. A. Ovrut, *Supersymmetric Extension of the SU(3) x SU(2) x U(1) Model*, Phys. Lett. **B113** (1982) 175.

[23] M. Dine and A. E. Nelson, *Dynamical supersymmetry breaking at low-energies*, Phys. Rev. **D48** (1993) 1277–1287, arXiv:hep-ph/9303230.

[24] M. Dine, A. E. Nelson, and Y. Shirman, *Low-energy dynamical supersymmetry breaking simplified*, Phys. Rev. **D51** (1995) 1362–1370, arXiv:hep-ph/9408384.

[25] M. Dine, A. E. Nelson, Y. Nir, and Y. Shirman, *New tools for low-energy dynamical supersymmetry breaking*, Phys. Rev. **D53** (1996) 2658–2669, arXiv:hep-ph/9507378.

[26] C. Petersson, A. Romagnoni, and R. Torre, *Higgs Decay with Monophoton + MET Signature from Low Scale Supersymmetry Breaking*, JHEP **1210** (2012) 016, arXiv:1203.4563 [hep-ph].

[27] N. Craig, D. Green, and A. Katz, *(De)Constructing a Natural and Flavorful Supersymmetric Standard Model*, JHEP **1107** (2011) 045, arXiv:1103.3708 [hep-ph].

[28] R. Auzzi, A. Giveon, and S. B. Gudnason, *Flavor of quiver-like realizations of effective supersymmetry*, JHEP **1202** (2012) 069, arXiv:1112.6261 [hep-ph].

[29] C. Csaki, L. Randall, and J. Terning, *Light Stops from Seiberg Duality*, Phys.Rev. **D86** (2012) 075009, arXiv:1201.1293 [hep-ph].

[30] G. Larsen, Y. Nomura, and H. L. Roberts, *Supersymmetry with Light Stops*, JHEP **1206** (2012) 032, arXiv:1202.6339 [hep-ph].

[31] N. Craig, S. Dimopoulos, and T. Gherghetta, *Split families unified*, JHEP **1204** (2012) 116, arXiv:1203.0572 [hep-ph].

[32] J. Ellis, J. F. Gunion, H. E. Haber, L. Roszkowski, and F. Zwirner, *Higgs bosons in a nonminimal supersymmetric model*, Phys. Rev. D **39** (1989) 844–869.

[33] ATLAS Collaboration, *The ATLAS Experiment at the CERN Large Hadron Collider*, JINST **3** (2008) S08003.

[34] J. Alwall, M. Herquet, F. Maltoni, O. Mattelaer, and T. Stelzer, *MadGraph 5 : Going Beyond*, JHEP **1106** (2011) 128, arXiv:1106.0522 [hep-ph].

[35] T. Sjöstrand, S. Mrenna, and P. Z. Skands, *A Brief Introduction to PYTHIA 8.1*, Comput.Phys.Commun. **178** (2008) 852–867, arXiv:0710.3820 [hep-ph].

[36] J. Pumplin, D. Stump, J. Huston, H. Lai, P. M. Nadolsky, et al., *New generation of parton distributions with uncertainties from global QCD analysis*, JHEP **0207** (2002) 012, arXiv:hep-ph/0201195 [hep-ph].

[37] J. M. Campbell, R. K. Ellis, and C. Williams, *Vector boson pair production at the LHC*, JHEP **1107** (2011) 018, arXiv:1105.0020 [hep-ph].

[38] K. Arnold, J. Bellm, G. Bozzi, M. Brieg, F. Campanario, et al., *VBFNLO: A Parton Level Monte Carlo for Processes with Electroweak Bosons – Manual for Version 2.5.0*, arXiv:1107.4038 [hep-ph].

[39] M. L. Mangano, M. Moretti, F. Piccinini, R. Pittau, and A. D. Polosa, *ALPGEN, a generator for hard multiparton processes in hadronic collisions*, JHEP **0307** (2003) 001, arXiv:hep-ph/0206293 [hep-ph].

[40] J. Butterworth, J. R. Forshaw, and M. Seymour, *Multiparton interactions in photoproduction at HERA*, Z.Phys. **C72** (1996) 637–646, arXiv:hep-ph/9601371 [hep-ph].

[41] T. Gleisberg, S. Hoeche, F. Krauss, M. Schonherr, S. Schumann, et al., *Event generation with SHERPA 1.1*, JHEP **0902** (2009) 007, arXiv:0811.4622 [hep-ph].

[42] S. Catani, L. Cieri, G. Ferrera, D. de Florian, and M. Grazzini, *Vector boson production at hadron colliders: a fully exclusive QCD calculation at NNLO*, Phys.Rev.Lett. **103** (2009) 082001, arXiv:0903.2120 [hep-ph].

[43] H.-L. Lai, M. Guzzi, J. Huston, Z. Li, P. M. Nadolsky, et al., *New parton distributions for collider physics*, Phys.Rev. **D82** (2010) 074024, arXiv:1007.2241 [hep-ph].

[44] S. Frixione, E. Laenen, P. Motylinski, and B. R. Webber, *Single-top production in MC@NLO*, Journal of High Energy Physics **2006** no. 03, (2006) 092. http://stacks.iop.org/1126-6708/2006/i=03/a=092.

[45] S. Frixione and B. R. Webber, *Matching NLO QCD computations and parton shower simulations*, JHEP **0206** (2002) 029, arXiv:hep-ph/0204244 [hep-ph].

[46] ATLAS Collaboration, *Search for Higgs boson decays to a photon and a Z boson in pp collisions at $\sqrt{s}$=7 and 8 TeV with the ATLAS detector*, Phys.Lett. **B732** (2014) 8–27, arXiv:1402.3051 [hep-ex].

[47] The GEANT4 Collaboration, S. Agostinelli *et al.*, *GEANT4: A simulation toolkit*, Nucl. Instrum. Meth. **A506** (2003) 250.

[48] *The ATLAS Simulation Infrastructure*, European Physical Journal C **70** (2010) 823–874, arXiv:1005.4568 [physics.ins-det].

[49] ATLAS Collaboration, *The simulation principle and performance of the ATLAS fast calorimeter simulation FastCaloSim*, ATL-PHYS-PUB-2010-013 (2010). http://cds.cern.ch/record/1300517.

[50] ATLAS Collaboration, *Expected photon performance in the ATLAS experiment*, ATL-PHYS-PUB-2011-007. http://cdsweb.cern.ch/record/1345329.

[51] ATLAS Collaboration, *Measurements of the photon identification efficiency with the ATLAS detector using 4.9 fb^{-1} of pp collision data collected in 2011*, ATLAS-CONF-2012-123. http://cds.cern.ch/record/1473426.

[52] ATLAS Collaboration, *Measurement of the inclusive isolated prompt photon cross section in pp collisions at sqrt(s) = 7 TeV with the ATLAS detector*, Phys.Rev. **D83** (2011) 052005, arXiv:1012.4389 [hep-ex].

[53] ATLAS Collaboration, *Electron reconstruction and identification efficiency measurements with the ATLAS detector using the 2011 LHC proton-proton collision data*, Eur.Phys.J. **C74** no. 7, (2014) 2941, arXiv:1404.2240 [hep-ex].

[54] ATLAS Collaboration, *Electron efficiency measurements with the ATLAS detector using the 2012 LHC proton-proton collision data*, ATLAS-CONF-2014-032. http://cds.cern.ch/record/1706245.

[55] ATLAS Collaboration, *Measurement of the muon reconstruction performance of the ATLAS detector using 2011 and 2012 LHC proton-proton collision data*, arXiv:1407.3935.

[56] M. Cacciari, G. P. Salam, and G. Soyez, *The anti-k_T jet clustering algorithm*, JHEP **04** (2008) 063.

[57] ATLAS Collaboration, *Pile-up subtraction and suppression for jets in ATLAS*, ATLAS-CONF-2013-083 (2013). http://cds.cern.ch/record/1570994.

[58] ATLAS Collaboration, *Performance of Missing Transverse Momentum Reconstruction in Proton-Proton Collisions at 7 TeV with ATLAS*, Eur.Phys.J. **C72** (2012) 1844, arXiv:1108.5602 [hep-ex].

[59] ATLAS Collaboration, *Performance of the ATLAS Electron and Photon Trigger in p-p Collisions at sqrts = 7 TeV in 2011*, ATLAS-CONF-2012-048 (2012). http://cds.cern.ch/record/1450089.

[60] ATLAS Collaboration, *Jet energy measurement and its systematic uncertainty in proton-proton collisions at $\sqrt{s}$ = 7 TeV with the ATLAS detector*, Eur.Phys.J. **C75** no. 1, (2015) 17, arXiv:1406.0076 [hep-ex].

[61] A. L. Read, *Presentation of search results: the CL s technique*, Journal of Physics G: Nuclear and Particle Physics **28** no. 10, (2002) 2693. http://stacks.iop.org/0954-3899/28/i=10/a=313.

[62] M. Baak, G. Besjes, D. Cote, A. Koutsman, J. Lorenz, et al., *HistFitter software framework for statistical data analysis*, arXiv:1410.1280 [hep-ex].